

# Low Energy Quantum System Simulation

Peter Cho and Karl Berggren

Lincoln Laboratory

Massachusetts Institute of Technology

Lexington, MA 02420

## Abstract

A numerical method for solving Schrödinger's equation based upon a Baker-Campbell-Hausdorff (BCH) expansion of the time evolution operator is presented herein. The technique manifestly preserves wavefunction norm, and it can be applied to problems in any number of spatial dimensions. We also identify a particular dimensionless ratio of potential to kinetic energies as a key coupling constant. This coupling establishes characteristic length and time scales for a large class of low energy quantum states, and it guides the choice of step sizes in numerical work. Using the BCH method in conjunction with an imaginary time rotation, we compute low energy eigenstates for several quantum systems coupled to non-trivial background potentials. The approach is subsequently applied to the study of 1D propagating wave packets and 2D bound state time development. Failures of classical expectations uncovered by simulations of these simple systems help develop quantum intuition.

Finally, we investigate the response of a Superconducting Quantum Interference Device (SQUID) to a time dependent potential. We discuss how to engineer the potential's energy and time scales so that the SQUID acts as a quantum NOT gate. The notional simulation we present for this gate provides useful insight into the design of one candidate building block for a quantum computer.

10/03

---

This work is sponsored by the Air Force Office of Scientific Research under Air Force Contract F19628-00-C-002. Opinions, interpretations, conclusions, and recommendations are those of the authors and are not necessarily endorsed by the United States Government.

## 1. Introduction

In this article, we study the low energy behavior of a quantum system that interacts with an external classical background. We specifically focus upon numerically simulating the evolution of a system with just a few degrees of freedom. Its characteristic time scales are generally assumed to be short compared with the background's, yet its typical velocities are required to be low compared to the speed of light. The dynamics of the quantum system are then accurately described by the non-relativistic Schrödinger equation <sup>1</sup>

$$i\frac{\partial}{\partial t}|\psi\rangle = \mathbf{H}(t)|\psi\rangle. \quad (1.1)$$

Here the “ket”  $|\psi\rangle$  denotes an abstract vector in a Hilbert space that is in one-to-one correspondence with the physical state of the system.

The system's time evolution is governed by the Hamiltonian

$$\mathbf{H}(t) = \vec{\mathbf{P}}^2 + V(\vec{\mathbf{X}}, t) \quad (1.2)$$

which is a sum of kinetic and potential energy terms. We absorb an inverse mass coefficient into  $\vec{\mathbf{P}}^2$  so that the kinetic operator has unit normalization. The potential term summarizes the classical background's effect on the quantum system. The corresponding reaction of the background to the system is ignored in Schrödinger's equation. The time dependence of  $V$  consequently represents a fixed input rather than a dynamically determined output.

If the potential is an arbitrary function of time, the Hamiltonian evaluated at some time  $t_1$  typically does not commute with the Hamiltonian evaluated at another time  $t_2$ . The formal solution to Schrödinger's equation

$$|\psi(t)\rangle = \mathbf{U}(t)|\psi(0)\rangle \quad (1.3)$$

then involves the unitary time evolution operator given by Dyson's formula

$$\mathbf{U}(t) = T \exp \left[ -i \int_0^t \mathbf{H}(t') dt' \right] \quad (1.4a)$$

$$= 1 + \sum_{n=1}^{\infty} (-i)^n \int_0^t dt_1 \int_0^{t_1} dt_2 \cdots \int_0^{t_{n-1}} dt_n \mathbf{H}(t_1) \mathbf{H}(t_2) \cdots \mathbf{H}(t_n). \quad (1.4b)$$

---

<sup>1</sup> We work with units where  $\hbar = 1$ . We also use bold-face symbols to denote abstract quantum operators.

The  $T$  symbol in (1.4a) indicates that the exponential is time ordered. As the series expansion in (1.4b) explicitly demonstrates, time ordering forces the temporally latest Hamiltonian factors to appear on the left. Given the complexity of (1.4), it is little surprise that the number of time dependent problems for which  $\mathbf{U}(t)$  can be evaluated in closed form is small.

If the classical background is independent of time, the evolution operator reduces to

$$\mathbf{U}(t) = \exp(-i\mathbf{H}t). \quad (1.5)$$

This exponentiated sum of non-commuting  $\vec{\mathbf{P}}^2$  and  $V(\vec{\mathbf{X}})$  operators can be decomposed into a product of exponentials via the Baker-Campbell-Hausdorff (BCH) expansion:

$$\mathbf{U}(t) = e^{O(t^4)} \times e^{-\frac{1}{3}(-it)^3 [V(\vec{\mathbf{X}}), [V(\vec{\mathbf{X}}), \vec{\mathbf{P}}^2]]} e^{\frac{1}{6}(-it)^3 [[V(\vec{\mathbf{X}}), \vec{\mathbf{P}}^2], \vec{\mathbf{P}}^2]} e^{-\frac{1}{2}(-it)^2 [V(\vec{\mathbf{X}}), \vec{\mathbf{P}}^2]} e^{-itV(\vec{\mathbf{X}})} e^{-it\vec{\mathbf{P}}^2}. \quad (1.6)$$

Since the adjoint for each exponential factor equals its matrix inverse, this decomposition manifestly preserves unitarity.

Although we are ultimately interested in simulating the response of quantum systems to time varying backgrounds, we initially restrict our attention to problems where the potential is not a function of time. Expansion (1.6) then provides a practical means for evolving state vectors on a computer. For example, one readily finds

$$\psi(\vec{x}, t) = \langle \vec{x} | \psi(t) \rangle = e^{-itV(\vec{x})} \mathcal{F}^{-1} \left( e^{-it\vec{p}^2} \mathcal{F}(\psi(\vec{x}, 0)) \right) + O(t^2) \quad (1.7a)$$

if just the leading exponential factors appearing on the right of (1.6) are retained. Here  $\mathcal{F}$  and  $\mathcal{F}^{-1}$  denote Fourier and inverse Fourier transform operations which are defined in Appendix A. If the next-to-leading exponentiated commutator is kept in the BCH decomposition of  $\mathbf{U}(t)$ , a more accurate evolution formula can be derived using operator identities listed in Appendix A:

$$\psi(\vec{x}, t) = e^{\frac{1}{2}t^2 \nabla^2 V(\vec{x}') - itV(\vec{x}')} \mathcal{F}^{-1} \left( e^{-it\vec{p}^2} \mathcal{F}(\psi(\vec{x}, 0)) \right) + O(t^3) \quad (1.7b)$$

with  $\vec{x}' = \vec{x} + t^2 \nabla V(\vec{x})$ . For our simulation work, we include the next-to-next-to-leading exponentiated nested commutator factors shown in eqn. (1.6). As the resulting generalization of (1.7b) is complicated and un-illuminating, we relegate it to Appendix B.

Our numerical approach to solving Schrödinger’s equation is a variant of exponentiated split operator methods that have been explored by several authors in the past [1,2]. It can be implemented in any number of spatial dimensions via efficient Fast Fourier Transform (FFT) codes unlike other matrix inversion algorithms which become unwieldy beyond one dimension [3]. The price we pay for such generality is having to Fourier transform back and forth between momentum and position space. As in all split operator approaches, such transforming is computationally expensive. So while others have studied more complicated decompositions of  $\mathbf{U}(t)$  that yield higher temporal order accuracy per time step [4,5], we prefer to work with the simpler evolution formulas in (1.7) and their subleading generalizations which minimize the number of transforms that must be performed.<sup>2</sup>

The outline for our article is as follows. In section 2, we identify a particular energy ratio as a dimensionless coupling constant that establishes characteristic length and time scales for several low energy quantum systems. For large values of this coupling, dimensional analysis helps guide the choice of FFT bin sizes needed to implement our BCH evolution algorithm. In section 3, we discuss a simple technique based upon an imaginary time rotation for projecting out low energy eigenstates from trial wavefunctions. The method is demonstrated to reproduce known spectra for analytically soluble 1D models and to yield consistent eigenfunctions for analytically intractable 2D systems. In section 4, we investigate Gaussian wavepacket propagation on three different backgrounds. As we shall see, the quantum motion of a packet inside a box is, at first glance, a surprise. In section 5, we simulate the response of a Superconducting Quantum Interference Device (SQUID) to a time varying potential. By judiciously modulating SQUID parameters, this device can be forced to act as a quantum NOT gate. Finally we summarize our findings in section 6 and close with some thoughts on future simulation work for quantum computer design.

## 2. Naive dimensional analysis

It is generally a good practice to scale out all dimensionful parameters from Schrödinger’s equation in order to gain qualitative insight into the quantum system it describes. Once dimensionful quantities have been removed, Schrödinger’s equation can

---

<sup>2</sup> According to the authors of ref. [6] who surveyed several different propagation schemes, it is unclear whether the gain in accuracy achieved by higher order symmetric expansions of  $\mathbf{U}(t)$  is offset by the considerably greater numerical effort required to implement such schemes.

only depend upon dimensionless ratios whose values relative to unity encode non-trivial physics information. In particular, these ratios act as coupling constants which govern the strength of the interaction between the quantum system and its classical background.

In order to derive a dimensionless form of Schrödinger's equation, we first restore all dimensionful parameters within Hamiltonian (1.2) and project it onto the position basis:

$$H(t) = \frac{-\hbar^2}{2m} \frac{\partial^2}{\partial \vec{x}^2} + V(\vec{x}, t). \quad (2.1)$$

We next express the position vector  $\vec{x}$  as the product of some arbitrary unit of length  $\ell$  and a dimensionless vector  $\vec{\beta}$ :

$$\vec{x} \equiv \ell \vec{\beta}.$$

The energy  $K_0 = \hbar^2/2m\ell^2$  is subsequently scaled out from the kinetic term in (2.1), and it is used to relate dimensionful time  $t$  to its dimensionless counterpart  $\tau$ :

$$t = \frac{\hbar}{K_0} \tau.$$

We also rewrite the potential term as another energy  $V_0$  times a function of  $\vec{\beta}$  and  $\tau$ :

$$V(\vec{x}, t) = V_0 U(\vec{\beta}, \tau).$$

The ratio

$$\mathcal{H} \equiv \frac{H}{K_0} = -\frac{\partial^2}{\partial \vec{\beta}^2} + \alpha U(\vec{\beta}, \tau) \quad (2.2)$$

with  $\alpha \equiv V_0/K_0$  then enters into the dimensionless Schrödinger equation

$$i \frac{\partial}{\partial \tau} \psi(\vec{\beta}, \tau) = \mathcal{H}(\tau) \psi(\vec{\beta}, \tau).$$

We work with version (2.2) of the Hamiltonian in all numerical simulations.

If the classical background is complicated, it is generally characterized by several length scales of different magnitudes. The potential is then implicitly a function of multiple length scale ratios:

$$U = U\left(\vec{\beta}, \tau; \frac{L}{L'}, \frac{L}{L''}, \dots\right).$$

Observable expectation values can depend in complicated ways upon  $\alpha$  and these dimensionless ratios. In this situation, naive dimensional analysis cannot be used to establish physical properties of low energy quantum systems such as their typical wavefunction spreads or oscillation frequencies.

But for the important special case where the background is characterized by a single length, dimensional considerations do fix the dependence of system scales upon the  $\alpha$  coupling. For example, consider an oscillator with Hamiltonian

$$\mathcal{H} = -\frac{\partial^2}{\partial \vec{\beta}^2} + \alpha (\vec{\beta}^2)^p. \quad (2.3)$$

According to the virial theorem, the kinetic and potential energies of the oscillator's low lying states are balanced on average:

$$\langle K \rangle = p \langle V \rangle. \quad (2.4)$$

The states' characteristic length and time consequently scale with  $\alpha$  as

$$L \sim (\alpha p)^{-\frac{1}{2p+2}} \quad T \sim (\alpha p)^{-\frac{1}{p+1}}, \quad (2.5a)$$

while their momentum and energy are inversely related to  $L$  and  $T$ :

$$P \sim (\alpha p)^{\frac{1}{2p+2}} \quad E \sim (\alpha p)^{\frac{1}{p+1}}. \quad (2.5b)$$

Note in particular that  $L \rightarrow 0$  as  $\alpha \rightarrow \infty$ . As one would intuitively expect, an oscillator's wavefunction becomes more tightly concentrated about the potential's minimum as the potential's walls grow more steep.

Consider next potentials such as  $U = -\vec{\beta}^2 + \vec{\beta}^4$  or  $U = \cos \vec{\beta}^2$  that possess non-vanishing quadratic terms at their minima. In the large  $\alpha$  limit, self-consistent dimensional analysis demonstrates that the scaling behavior in (2.5a, b) continues to hold with power  $p = 1$ . As the wavefunction becomes concentrated about the minimum point, it effectively senses only the leading quadratic term in the potential's expansion about the minimum. The low energy spectra for a large class of systems therefore look like that for a harmonic oscillator as  $\alpha \rightarrow \infty$ . As an illustrative example of this general behavior, we plot in fig. 1 the first ten eigenvalues for periodic energy eigenstates of a one-dimensional cosine potential with  $\alpha = 100$ . Though the eigenstates occur in nearly degenerate parity doublets, the familiar harmonic oscillator level spacing is evident in the figure.

These elementary dimensional analysis considerations help guide the practical choice of FFT bin sizes needed to numerically implement the Fourier transforms in eqns. (1.7a, b) and their subleading generalizations:

$$\delta\beta = \frac{\alpha^{-1/4}}{\sqrt{N}} \quad \delta\kappa = \frac{\alpha^{1/4}}{\sqrt{N}}. \quad (2.6)$$

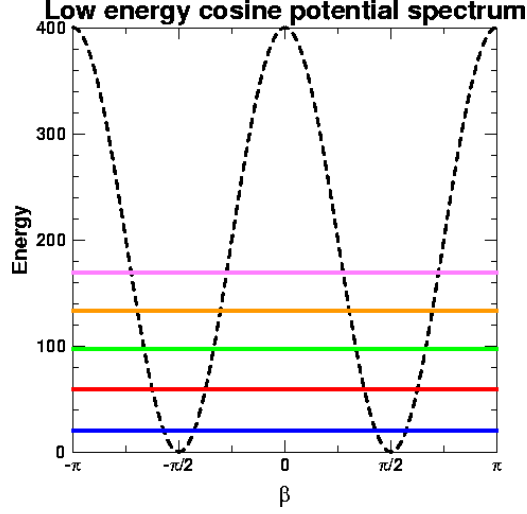


Fig. 1: Lowest ten eigenvalues for periodic eigenstates of a quantum system coupled to a  $U(\beta) = 2 + 2 \cos(2 \beta)$  potential with strength  $\alpha = 100$ . The eigenstates occur in parity even and odd pairs, but each pair's splitting is not resolvable on this plot's scale. The first four excited pair energies are in the ratios 2.97, 4.89, 6.76 and 8.56 relative to the ground state energy. Recall the corresponding harmonic oscillator energy ratios are 3, 5, 7 and 9.

In order to keep the position and momentum spaces on an equal footing, we set both  $\delta\beta$  and its dimensionless momentum analog  $\delta\kappa$  inversely proportional to the square root of the total number of bins  $N$  in each spatial dimension. But we modulate the bins' magnitudes by fractional powers of  $\alpha$  to take into account generic systems' length and momentum scales. We likewise set the time step  $\delta\tau$  used to evolve Schrödinger's equation proportional to  $1/\sqrt{\alpha}$ . These scaling choices significantly improve simulation efficiency for strongly coupled quantum systems.

### 3. Energy eigenstate evaluation

One of the most important properties of a quantum system is its low energy spectrum. It is natural to consider initially preparing a system in its ground state or in a superposition of a few excited states. We then want to simulate how it evolves over time and reacts to changes in the classical background. In order to carry out this program, we first need to compute the system's low energy eigenstates.

To begin, we center  $U(\vec{\beta})$  about the origin  $\vec{\beta} = \vec{0}$ . Translating the potential is especially important for simulating wavefunction evolution on periodic manifolds like  $S^1$

(circle in 1D) or  $S^1 \times S^1$  (torus in 2D). The periodicity of the FFT can be exploited to numerically solve Schrödinger's equation on such manifolds for states with periodic boundary conditions. We therefore restrict the domain for  $\vec{\beta}$  to a single period in each spatial dimension for which  $U(\vec{\beta})$  is periodic.

We next construct a trial wavefunction in position space for each low-lying energy state. In one spatial dimension, the parity of the ground state corresponding to a symmetric potential  $U(\beta) = U(-\beta)$  is always even. Moreover, successive non-degenerate energy states labeled by principle quantum number  $n$  have alternating  $(-1)^n$  parity assignments. So for a potential which is aperiodic in  $\beta$ , we take the  $n^{\text{th}}$  eigenstate's trial wavefunction to be proportional to  $\beta^{(n \bmod 2)} \exp(-\beta^2)$ . If  $U(\beta)$  is periodic on the other hand, we set  $\psi_{\text{trial}}$  proportional to  $\beta^{(n \bmod 2)} U(\beta)^{-1}$ . These initial guesses are generally useful even when the potential does not exhibit a perfect reflection symmetry. Moreover, they correctly place the bulk of low energy wavefunction content in valley regions of the potential.

Similar considerations motivate the choice of trial wavefunctions in higher spatial dimensions. For example in 2D, we set the trial wavefunction for the energy eigenstate labeled by principle quantum numbers  $m$  and  $n$  proportional to  $\beta_x^{(m \bmod 2)} \beta_y^{(n \bmod 2)} U(\beta_x, \beta_y)^{-1}$  if the potential is periodic in both  $\beta_x$  and  $\beta_y$ . On the other hand, we take  $\psi_{\text{trial}}$  to be a two-dimensional Gaussian modulated by  $\beta_x^{(m \bmod 2)} \beta_y^{(n \bmod 2)}$  if the potential has infinite period.

Once a trial wavefunction for the ground state has been selected, it can be written as an *a priori* unknown superposition of the true ground state  $\psi_0$  and all other energy eigenstates with which it shares the same symmetry properties:

$$\psi_{\text{trial}}^{(0)}(\vec{\beta}, 0) = C_0 \psi_0(\vec{\beta}, 0) + \sum_{j>0} C_j \psi_j(\vec{\beta}, 0).$$

In order to distill  $\psi_0$  from this infinite sum, we iteratively evolve the trial state according to the imaginary time evolution operator  $e^{-\mathcal{H}\tau}$  using subleading generalizations of eqn. (1.7) with  $\tau \rightarrow -i\tau$ :

$$\psi_{\text{trial}}^{(0)}(\vec{\beta}, \tau) = C_0 e^{-E_0 \tau} \psi_0(\vec{\beta}, 0) + \sum_{j>0} C_j e^{-E_j \tau} \psi_j(\vec{\beta}, 0).$$

Following each timestep increment, the wavefunction is renormalized to preserve amplitude content. As the iteration proceeds, the trial wavefunction's excited energy state components become exponentially suppressed compared to the ground state term. Ultimately,  $\psi_{\text{trial}}^{(0)}$  relaxes to the true ground state

$$\psi_{\text{trial}}^{(0)}(\vec{\beta}, \tau) \xrightarrow{\tau \rightarrow \infty} \psi_0(\vec{\beta}, 0),$$



and its Hamiltonian expectation value approaches the genuine lowest energy eigenvalue:

$$\langle \psi_{\text{trial}}^{(0)}(\tau) | \mathcal{H} | \psi_{\text{trial}}^{(0)}(\tau) \rangle \xrightarrow{\tau \rightarrow \infty} E_0.$$

Once the ground state is known, we select a new trial wavefunction  $\psi_{\text{trial}}^{(1)}$ , compute its overlap with the lowest energy state and form the difference

$$\psi_{\text{reduced}} = \psi_{\text{trial}}^{(1)} - \langle \psi_0 | \psi_{\text{trial}}^{(1)} \rangle \psi_0.$$

We subsequently project out the first excited eigenstate from this reduced wavefunction by repeating the imaginary time evolution procedure described above for the ground state. By following this projection and evolution strategy, we can compute any energy eigenstate and eigenvalue so long as build-up of numerical inaccuracies does not become overwhelmingly large.

As a first sanity check on this procedure, we illustrate its results in fig. 2 for a 1D harmonic oscillator which couples with strength  $\alpha = 1$  to a quadratic potential. The numerically computed spectrum and eigenfunctions reproduce well-known analytic formulas. In order to recover dimensionful energies from the dimensionless eigenvalues shown in the figure, we need to multiply the latter by the energy  $K_0 = \frac{1}{2}\hbar^2/m\ell^2$  which we scaled out from Hamiltonian (2.2). Recalling  $V_0 = \frac{1}{2}m\omega^2\ell^2$  for a simple harmonic oscillator with natural frequency  $\omega$  and  $\alpha = V_0/K_0$ , we deduce  $K_0 = \hbar\omega/2$ . So the  $n^{\text{th}}$  state's dimensionless  $2n + 1$  eigenvalue matches onto the dimensionful oscillator energy  $E_n = (2n + 1)\hbar\omega/2$ .

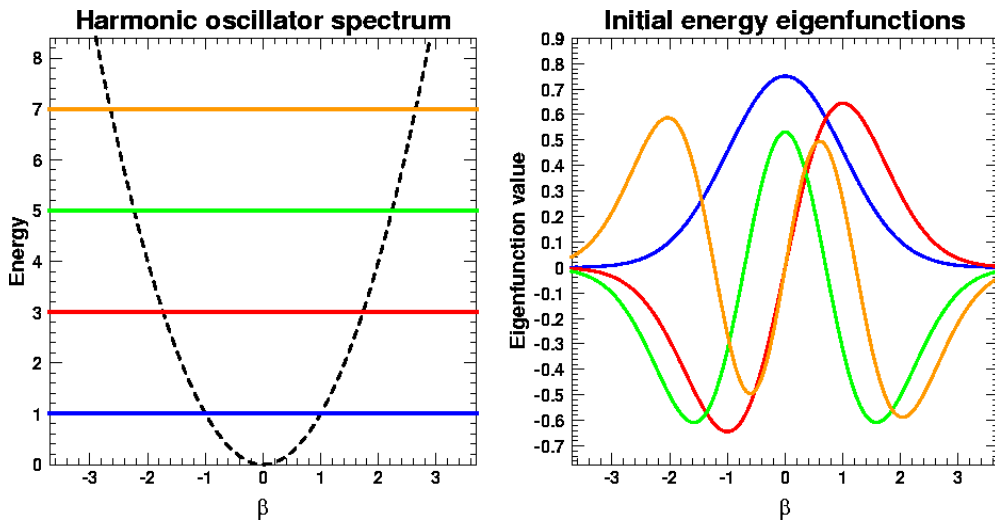


Fig. 2: Low energy eigenvalues and eigenstates for a harmonic oscillator with coupling  $\alpha = 1$  to a quadratic potential.

As a more challenging test, we apply our eigenstate evaluation algorithm to a system that interacts with potential  $U(\beta) = 2 + 2 \cos 2\beta$ . In this case, the Schrödinger problem maps onto Mathieu's differential equation:

$$\left[ \frac{\partial^2}{\partial \beta^2} + (E - 2\alpha) - 2\alpha \cos 2\beta \right] \psi(\beta) = 0. \quad (3.1)$$

As we have previously noted, the low energy spectrum for  $\alpha \gg 1$  looks like the harmonic oscillator's. On the other hand, known power series expressions for the eigenvalues of Mathieu's equation are convergent when  $\alpha \simeq O(1)$  [7]. We therefore set  $\alpha = 1$  and compare numerically derived eigenvalues with their power series counterparts in Table 1.

Some of the discrepancies between the analytic and numerical results shown in the table are attributable to power series truncation. In particular, we estimate an  $O(10^{-3})$  uncertainty in the zeroth and fourth analytic eigenvalues based upon the magnitudes of the last power series terms listed by Abramowitz and Stegun [7]. Unfortunately, we have no simple way to *a priori* quantify errors in our numerical eigenvalues. Nevertheless, the agreement between the two sets of energies is overall quite good for the first 11 periodic eigenstates.

As a final example, we consider a two-dimensional quantum system for which no analytic spectrum solution is known. It couples with unit strength to the dimensionless potential

$$U(\beta_x, \beta_y) = 3 + \cos 2\beta_y - 2 \cos \beta_x \cos \beta_y$$

plotted in fig. 3. Note that  $U$  remains invariant under  $\beta_x \leftrightarrow -\beta_x$  and  $\beta_y \leftrightarrow -\beta_y$  reflections, but not under  $\beta_x \leftrightarrow \beta_y$  exchange. The system's lowest three eigenvalues labeled by principle quantum numbers  $m$  and  $n$  equal  $E_{00} = 2.59$ ,  $E_{01} = 3.37$  and  $E_{10} = 3.79$ . Their associated eigenfunctions  $\psi_{00}$ ,  $\psi_{01}$  and  $\psi_{10}$  are respectively displayed in figs. 4a, 4b and 4c. As expected, the ground state's amplitude is concentrated in valley regions of the 2D potential, while its phase is everywhere uniform. In contrast, the first and second excited states exhibit node lines along the  $\beta_y = 0$  and  $\beta_x = 0$  axes, and their amplitudes on the two sides of these nodal separations are  $180^\circ$  out of phase. Most of the excited states' wavefunction densities avoid the potential's mountain terrain.

The magnitudes and relative phases of these eigenfunctions must be preserved as they evolve under the action of the unitary operator in (1.5). We have verified that these stationary wavefunction conditions are indeed maintained up to small numerical errors. Moreover, the states' energies remain constant as time proceeds. So although we cannot

Energy eigenstate	Analytic eigenvalue	Numerical eigenvalue
0	1.5457	1.5434
1	1.8897	1.8897
2	3.8591	3.8587
3	5.9170	5.9170
4	6.3704	6.3826
5	11.0477	11.0477
6	11.0784	11.1114
7	18.0330	18.0329
8	18.0338	18.0958
9	27.0208	27.0209
10	27.0209	27.1204

Table. 1: Lowest 11 energy eigenvalues for a system with periodic wavefunction boundary conditions that is coupled to potential  $U(\beta) = 2 + 2 \cos(2 \beta)$  with strength  $\alpha = 1$ . The analytic eigenvalues are based upon power series solutions to Mathieu's equation [7].

directly compare the results in fig. 4 with analytic expressions, our confidence in their validity is high.

It is interesting to investigate time dependent interference between combinations of the stationary states. In fig. 5a, we display the initial superposition

$$\psi(\beta_x, \beta_y) = \frac{1}{\sqrt{2}} \left( \psi_{00}(\beta_x, \beta_y) + \psi_{01}(\beta_x, \beta_y) \right) \quad (3.2)$$

of the ground and first excited states at  $\tau = 0$ . The dimensionless beat period for this simple combination equals  $T_{\text{beat}} = 2\pi/(E_{01} - E_{00}) = 8.1$ . In fig. 5b and fig. 5c, we plot  $\psi(\beta_x, \beta_y)$  at approximately the quarter and half way points through the beat cycle.

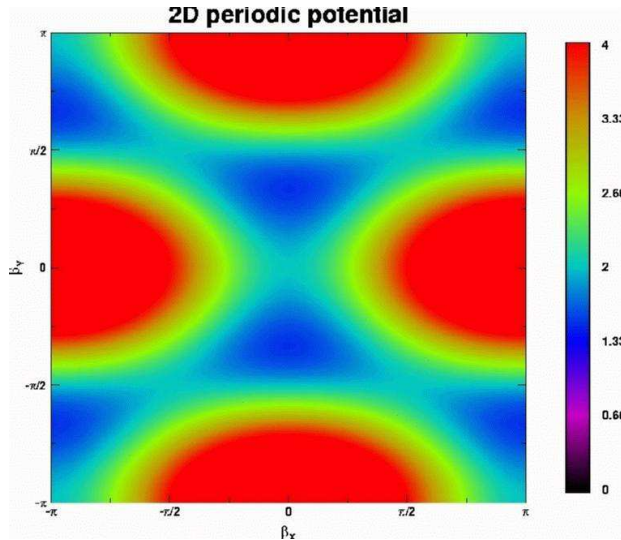


Fig. 3: The two-dimensional periodic potential  $U(\beta_x, \beta_y) = 3 + \cos 2\beta_y - 2 \cos \beta_x \cos \beta_y$ .

Amplitude density tunneling between potential valley regions for this superposition state is evident in the sequence of wavefunction snapshots shown in the figure.

One could proceed to examine the time dependence of more complicated superposition states. But rather than continue the bound state discussion, we turn at this point to investigate propagating states which exhibit qualitatively different quantum phenomena.

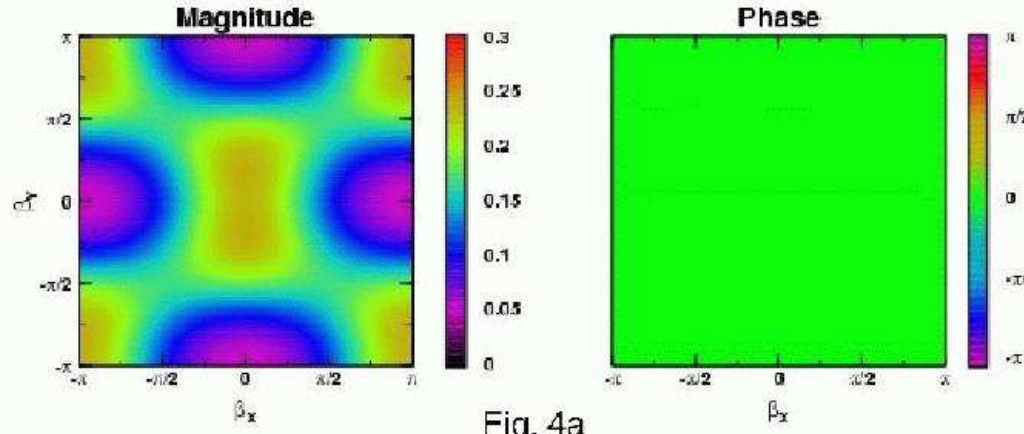


Fig. 4a

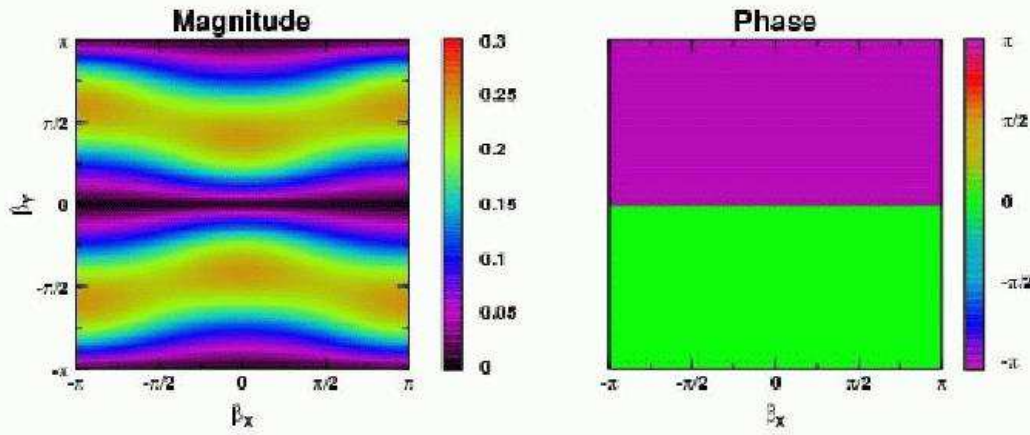


Fig. 4b

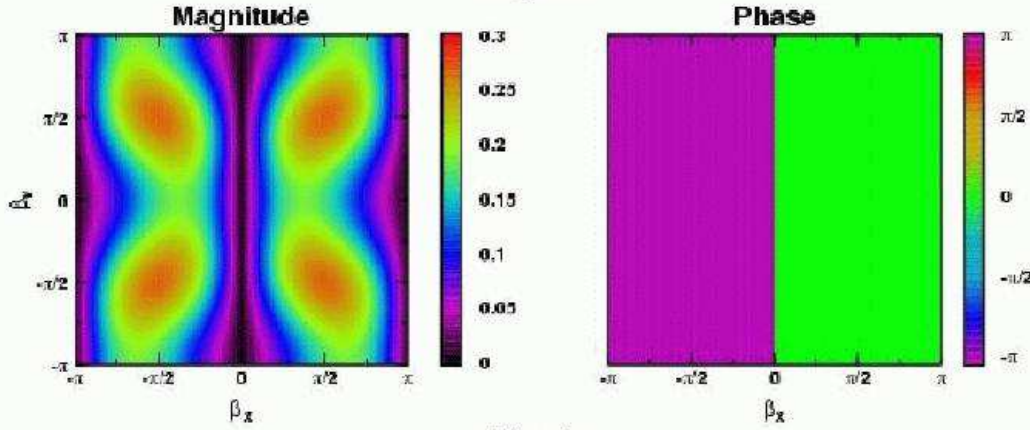


Fig. 4c

Fig. 4: Lowest three energy eigenstates corresponding to the periodic potential in fig. 3.

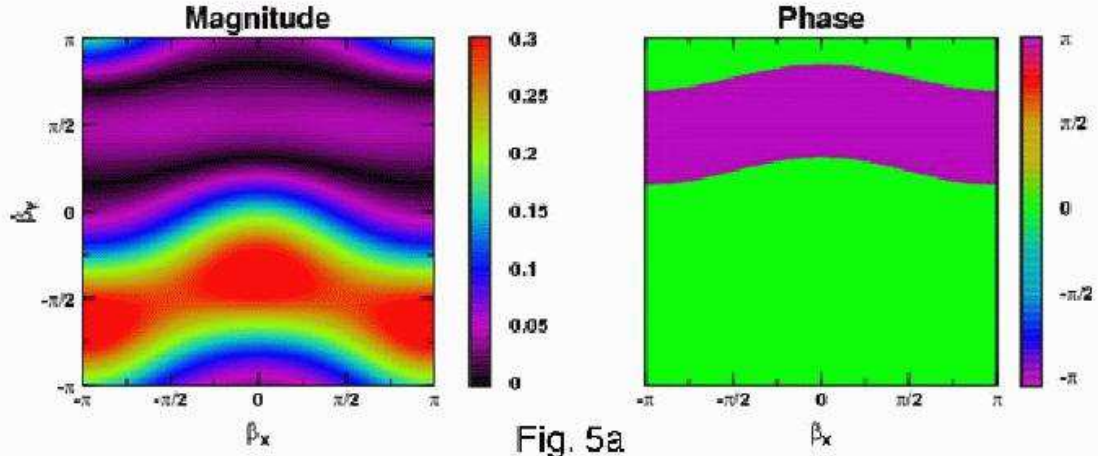


Fig. 5a

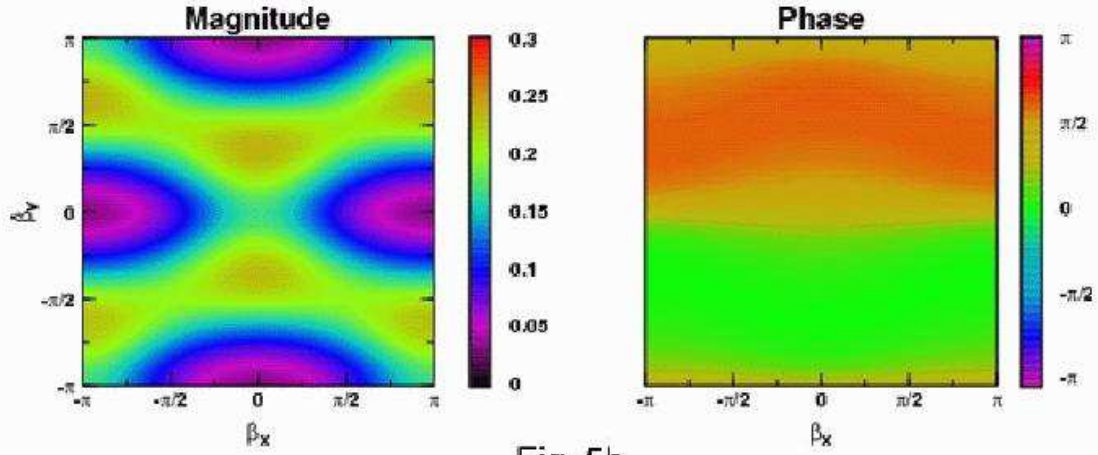


Fig. 5b

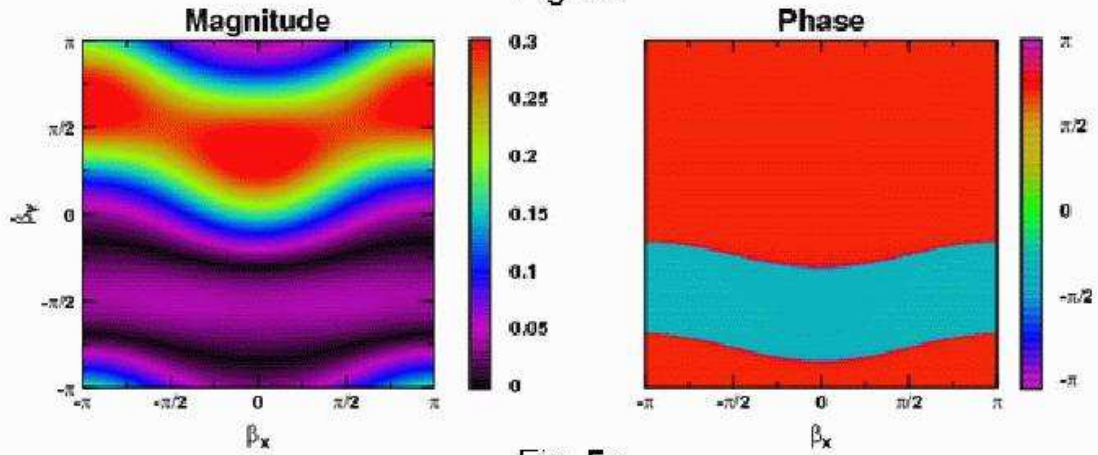


Fig. 5c

Fig. 5: (a) Initial superposition of the ground and first excited states from fig. 4. (b) Superposition at  $\tau \approx \frac{1}{4}T_{\text{beat}}$ . (c) Superposition at  $\tau \approx \frac{1}{2}T_{\text{beat}}$ .

#### 4. Gaussian wavepacket propagation

We start our exploration of propagating states by considering the well-known example of free Gaussian wavepacket evolution in one spatial dimension. The initial state is taken to have dimensionless mean position  $\beta_0$ , dimensionless standard deviation  $\sigma_0$  and dimensionless momentum  $k_0$ :

$$\psi(\beta, 0) = \left[ \frac{1}{2\pi\sigma_0^2} \right]^{1/4} \exp \left[ -\frac{(\beta - \beta_0)^2}{4\sigma_0^2} \right] \exp[ik_0\beta]. \quad (4.1)$$

For the simple case of free propagation, Schrödinger's equation can be solved analytically to determine the packet's time evolution:

$$\psi(\beta, \tau) = \left[ \frac{1}{2\pi\sigma^2(\tau)} \right]^{1/4} \exp \left[ -\frac{(\beta - \beta_0 - 2k_0\tau)^2}{4\sigma^2(\tau)} \right] \times (\text{phase terms}) \quad (4.2)$$

where

$$\sigma(\tau) = \sqrt{\sigma_0^2 + \left( \frac{\tau}{\sigma_0} \right)^2}. \quad (4.3)$$

Though the wavefunction's phase terms are exactly calculable, we choose not to explicitly list their ugly expressions here.

The mean motion of the packet

$$\langle \beta(\tau) \rangle = \beta_0 + 2k_0\tau \quad (4.4)$$

conforms with classical intuition.<sup>3</sup> On the other hand, the packet's spreading over time is unexpected from particle mechanics. In order to demonstrate that the origin of this diffusion is not purely a classical wave effect, we restore all dimensionful parameters in (4.3) and expand the packet's width in powers of  $\hbar$ :

$$s(t) = s_0 \sqrt{1 + \frac{\hbar^2 t^2}{4m^2 s_0^4}} = s_0 + O(\hbar^2). \quad (4.5)$$

In the classical  $\hbar \rightarrow 0$  limit, wavepacket diffusion does not occur. So it represents a genuine quantum phenomenon.

These analytic results for free Gaussian packet evolution can be reproduced by the numerical techniques described in the preceding sections. For example, we plot the mean

---

<sup>3</sup> Recall we have absorbed a factor of  $1/2m$  into our dimensionless Hamiltonian's kinetic term. If all dimensionful factors are restored, eqn. (4.4) reads  $\langle x(t) \rangle = x_0 + p_0 t/m$ .

position and standard deviation of a packet with  $\beta_0 = 0$ ,  $\sigma_0 = 1/\sqrt{2}$  and  $k_0 = 4$  as functions of time in fig. 6a. Numerical results shown in red are superposed for comparison on analytic results shown in green. Agreement between the two is clearly quite good.

We consider next numerically propagating wave packets for problems where closed form analytic formulas are difficult to obtain. In fig. 6b, the time dependent position and diffusion of a packet with the same dimensionless starting point, initial width and momentum as that in fig. 6a are displayed. However in this second example, the packet encounters an infinite wall located at  $\beta = 8$  as represented by the dashed blue line in the mean position figure. It bounces off with no penetration into the energetically forbidden region. During the time the packet interacts with the wall, the leading and trailing portions of its wavefunction interfere with each other. But after the encounter is finished, the packet's mean motion once again looks reasonably classical, and its diffusion is essentially unaffected by the interaction with the wall.

The motion of a wavepacket inside a box is much more curious. We again take the initial state to be the same as that in fig. 6a, and we graph its probability density in the first snapshot of fig. 7. Subsequent snapshots in fig. 7 depict the packet's evolution as it bounces between two infinite walls positioned at  $\beta = \pm 8$ . As time proceeds, the diffusion of the packet becomes so pronounced that it continuously interferes with itself everywhere inside the box. Once the packet completely fills the energetically allowed region, it no longer exhibits an identifiable peak or momentum flow. Consequently, its mean position decays over time to zero (see fig. 6c).

One might wonder whether this last result violates Ehrenfest's theorem which states that the laws of classical mechanics hold for quantum expectation values:

$$m \frac{d^2}{dt^2} \langle x \rangle = - \frac{d}{dx} \langle V(x) \rangle. \quad (4.6)$$

But as  $\langle V(x) \rangle \neq V(\langle x \rangle)$ , the wavepacket's mean position does *not* obey Newton's law of motion. So while a classical particle would indefinitely ricochet off the walls of the box, the quantum wavepacket's mean asymptotes instead to the center. The motion of a quantum packet trapped inside a box is thus highly non-classical.



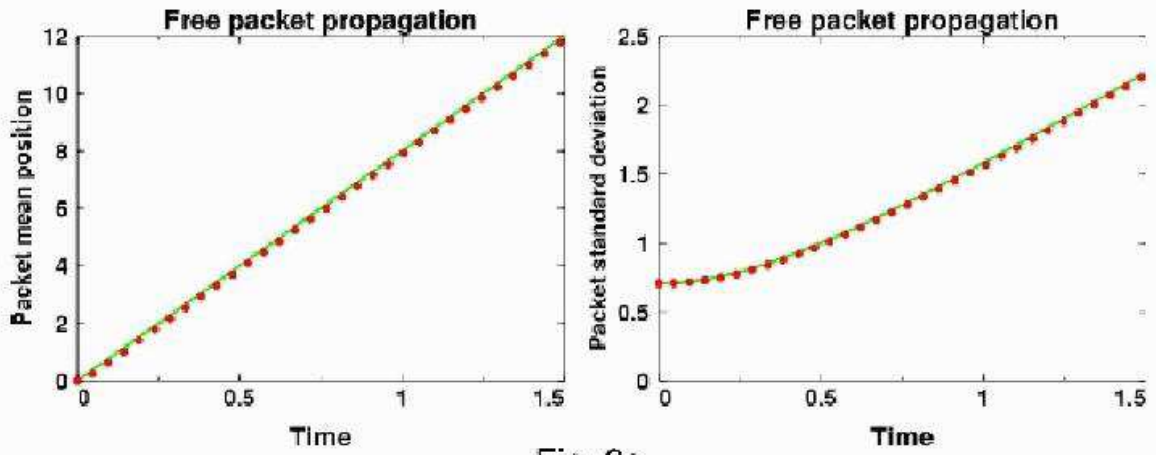


Fig. 6a

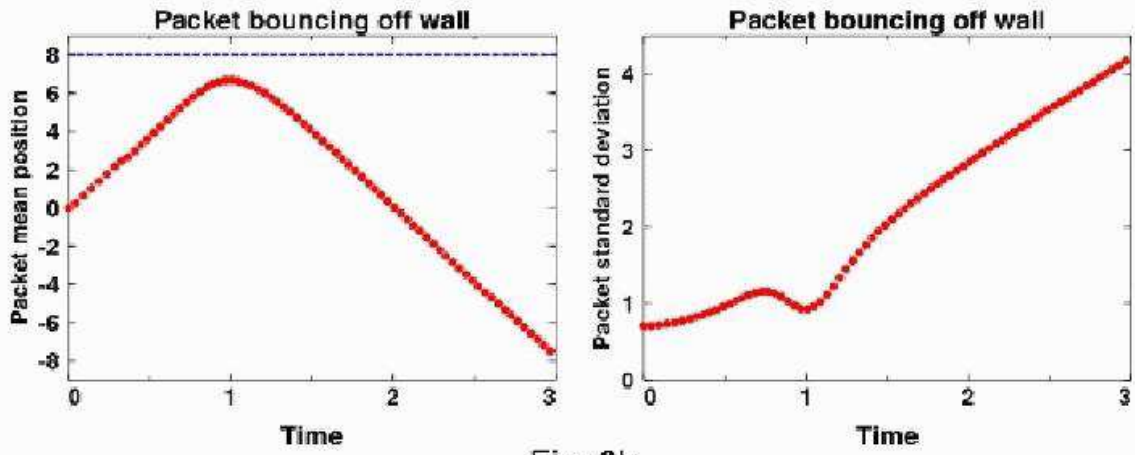


Fig. 6b

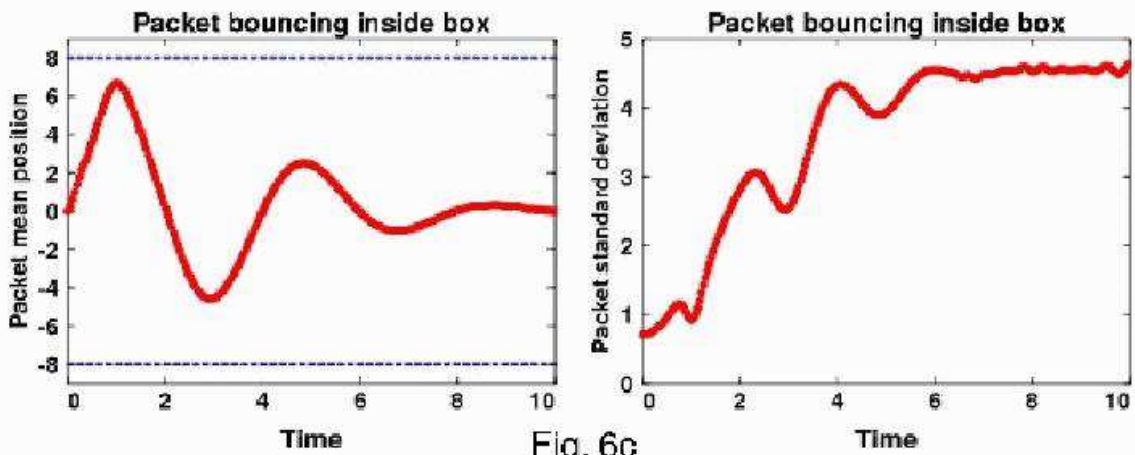


Fig. 6c

Fig. 6: Mean position and standard deviation as functions of time for a 1D Gaussian wavepacket (a) propagating in free space, (b) bouncing off a wall and (c) bouncing inside a box.

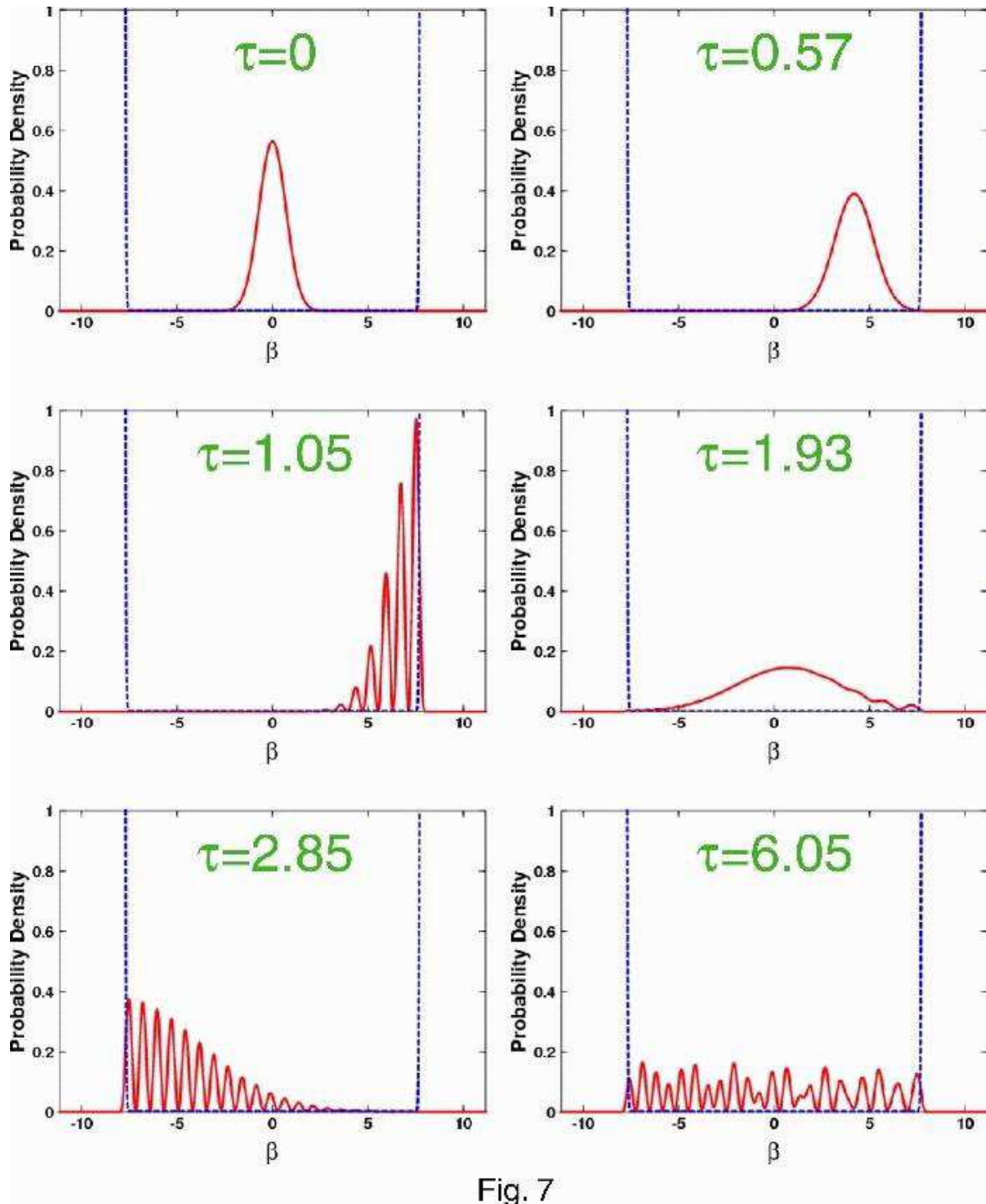


Fig. 7: Probability density snapshots of a 1D Gaussian wavepacket bouncing inside a box.

## 5. A notional quantum NOT gate

We have so far investigated the interactions between simple quantum systems with static classical backgrounds. Now we consider modulating a potential over time and measuring the system’s response. The spatial and temporal dependence of potentials corresponding to various experimental setups may be purposefully engineered to possess useful properties from an information theory standpoint. After a system is prepared in some initial state, its wavefunction is intentionally manipulated via a time varying potential. The system’s final-state wavefunction is subsequently read out and measured by the classical environment. This general program is currently of great interest for quantum computing applications. In this section, we examine the impact of a time dependent coupling upon one particular quantum system: the SQUID.

Superconducting Quantum Interference Devices presently represent one of the most promising candidate building blocks for quantum computers. SQUID circuits can theoretically support currents running clockwise and counterclockwise simultaneously. Recent experimental indications of such superposition states are beginning to demonstrate the validity of quantum mechanics on macroscopic scales [8,9] as well as the viability of SQUIDS as real-world qubits [10–12]. Moreover, SQUIDS are technologically attractive. These passive devices are small enough so that they can be mass produced on chips. Yet they are sufficiently large so that their quantum properties can be manipulated in a controlled fashion. SQUID design, fabrication and testing consequently represent active areas of research.

As the quantum mechanics of SQUIDS may not be familiar to some readers, we review the Hamiltonian  $\mathbf{H}_{\text{SQUID}}$  which governs their dynamics in subsection 5.1. The potential that enters into  $\mathbf{H}_{\text{SQUID}}$  looks like a double-well within certain regions of its parameter space. Wavefunction localization in one of the two wells may naturally be interpreted as a logical “true” or “false” signal. If the couplings in  $\mathbf{H}_{\text{SQUID}}$  are manipulated over time, coherent wavefunction movement from one well to the other can be controlled. So SQUID quantum mechanics has enough structure for these devices to act as quantum NOT gates.

We subsequently explore SQUID dynamics in subsection 5.2 using our simulation techniques. It is important to note again that the naive time dependent generalization of the evolution operator in (1.5)

$$\mathbf{U}(t)_{\text{naive}} = \exp\left[-i \int_0^t \mathbf{H}(t') dt'\right] \quad (5.1)$$

differs from the true propagator in (1.4) by commutator terms which enter at second order in the time step expansion:

$$\mathbf{U}(t)_{\text{true}} - \mathbf{U}(t)_{\text{naive}} = \frac{1}{2} \int_0^t dt_1 \int_0^{t_1} dt_2 [\mathbf{H}(t_1), \mathbf{H}(t_2)] + O(t^3). \quad (5.2)$$

These commutators render most numerical methods for solving Schrödinger's equation less accurate for time dependent backgrounds, and ours provides no exception to this general rule. But since we are more interested in rapidly gaining qualitative insight into SQUID experiment design than in achieving high numerical precision, we continue to use (1.7) and its subleading generalizations to propagate SQUID states interacting with time dependent potentials. We do, however, employ simple dynamic time step procedures to limit the accumulation of numerical errors.

### 5.1. The SQUID Hamiltonian

To begin the derivation of  $\mathbf{H}_{\text{SQUID}}$ , we sketch a cartoon of a Superconducting Quantum Interference Device in fig. 8. As the figure illustrates, a SQUID is simply a superconducting ring interrupted by a small insulator. A supercurrent of Cooper pairs flows around the ring and quantum mechanically tunnels through the junction. The nonlinear relationships between the insulator's current and voltage were worked out by Josephson in 1962 [13]. The insulator section acts as a nonlinear circuit element, and it is referred to as a Josephson junction.

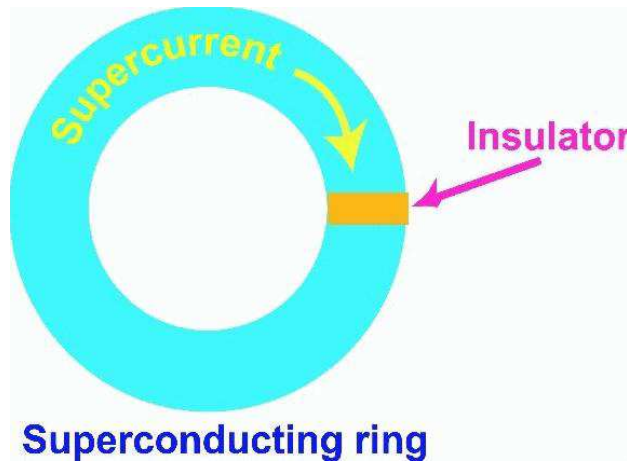


Fig. 8: An idealized SQUID pictured as a superconducting ring carrying a supercurrent that is interrupted by an insulator section.

Following Feynman [14], we let  $\psi(\vec{x})$  denote the wavefunction of a low energy Cooper pair within the ring. In the presence of a background classical electromagnetic field,  $\psi$  obeys a gauged Schrödinger equation. Without loss of generality, it may be decomposed as  $\psi = \sqrt{\rho}e^{i\phi}$  where  $\rho = \psi^*\psi$  is interpreted as Cooper pair probability density. Since  $\psi$  must be single-valued everywhere along the ring, its phase  $\phi$  must be a periodic function of  $\vec{x}$ .

Probability density  $\rho$  and its current counterpart  $\vec{\mathbf{J}}$  satisfy a gauged version of the familiar local conservation law  $d\rho/dt = -\vec{\nabla} \cdot \vec{\mathbf{J}}$ . This conservation requirement implies

$$\vec{\mathbf{J}} = \frac{1}{2m} \left[ \psi^* (-i\hbar \vec{\nabla} \psi) - \psi (-i\hbar \vec{\nabla} \psi^*) - 2(2e)\vec{\mathbf{A}}\psi^*\psi \right] = \frac{\hbar}{m} \left[ \vec{\nabla} \phi - \frac{2e}{\hbar} \vec{\mathbf{A}} \right] \rho$$

where  $\vec{\mathbf{A}}$  denotes the vector potential for the classical photon field. As all currents within a superconductor are spatially localized near its surface,  $\vec{\mathbf{J}}$  vanishes deep inside its interior. So

$$\vec{\nabla} \phi = \frac{2e}{\hbar} \vec{\mathbf{A}} \quad (5.3)$$

everywhere along a contour which lies buried in the SQUID ring (see fig. 9).



Fig. 9: Contour deep inside the superconducting ring along which  $\vec{\mathbf{J}} = 0$ . The total magnetic flux enclosed by the ring is proportional to the phase drop across the junction.

The phase drop across the junction can be related to the total magnetic flux that passes through the ring's hole by integrating (5.3) along the contour between its endpoints:

$$\begin{aligned} \phi &\equiv \phi_2 - \phi_1 = \int_1^2 \vec{\nabla} \phi \cdot d\vec{s} \\ &= \frac{2e}{\hbar} \int_1^2 \vec{\mathbf{A}} \cdot d\vec{s} \simeq \frac{2e}{\hbar} \oint \vec{\mathbf{A}} \cdot d\vec{s} = \frac{2e}{\hbar} \int (\vec{\nabla} \times \vec{\mathbf{A}}) \cdot d\vec{a} \\ &= \frac{2e}{\hbar} \Phi_{\text{total}} = \left( \frac{2\pi}{\Phi_0} \right) \Phi_{\text{total}}. \end{aligned} \quad (5.4)$$

The ratio  $\Phi_0 \equiv h/2e$  represents a fundamental unit of flux. Therefore, the junction phase drop counts the number of “fluxons” that thread the ring.

The total magnetic flux appearing in (5.4) is typically a sum of supercurrent-generated internal flux plus some applied external flux:  $\Phi_{\text{total}} = \Phi_{\text{int}} + \Phi_{\text{ext}}$ . The classical expression for the energy associated with  $\Phi_{\text{int}}$  and the ring’s geometrical self-inductance  $L$  motivates the first term in the SQUID’s quantum Hamiltonian:

$$\mathbf{H}_{\text{inductance}} = \frac{\Phi_{\text{int}}^2}{2L} = \frac{(\Phi_{\text{total}} - \Phi_{\text{ext}})^2}{2L} = \frac{(\Phi_0/2\pi)^2}{2L}(\phi^2 - \phi_0)^2.$$

In this formula, the phase offset is related to the external flux by (5.4):  $\phi_0 = (2\pi/\Phi_0)\Phi_{\text{ext}}$ .

A second contribution to  $\mathbf{H}_{\text{SQUID}}$  originates from the capacitance of the Josephson junction. The electric charge on the junction varies over time, for not every Cooper pair tunnels through the insulator. The classical energy associated with this charge motivates the second Hamiltonian term

$$\mathbf{H}_{\text{capacitance}} = \frac{\mathbf{Q}^2}{2C} = E_C \mathbf{n}^2.$$

The charge operator  $\mathbf{Q} = 2e\mathbf{n}$  effectively counts the number of pairs on the junction. When  $\mathbf{H}_{\text{capacitance}}$  is rewritten in terms of the dimensionless number operator  $\mathbf{n}$ , its overall scale is set by the Cooper pair capacitance energy  $E_C = (2e)^2/2C$ .

The Cooper pair number and phase operators are canonically conjugate to each other, and they satisfy the commutation relation  $[\mathbf{n}, \phi] = -i$ . In the  $\phi$  representation, the number operator  $\mathbf{n} \rightarrow -i\partial/\partial\phi$  is seen to be the infinitesimal generator of  $\phi$  translations. Similarly,  $\phi$  may be interpreted as the generator of  $\mathbf{n}$  translations. These observations are important for understanding the final contribution to the SQUID Hamiltonian

$$\mathbf{H}_{\text{junction}} = -\frac{E_J}{2} \sum_{n=0}^{\infty} \left\{ |n+1\rangle\langle n| + |n\rangle\langle n+1| \right\} \quad (5.5)$$

which describes the energy needed to transport a Cooper pair across the Josephson junction [15,16].

The quantum expression in (5.5) has no classical progenitor. Its prefactor is set by convention, while  $\mathbf{S}^+ \equiv \sum_{n=0}^{\infty} |n+1\rangle\langle n|$  and  $\mathbf{S}^- = (\mathbf{S}^+)^\dagger$  constitute raising and lowering operators.  $\mathbf{S}^\pm$  may alternatively be regarded as the finite translations  $e^{\mp i\phi} \xrightarrow{n \text{ rep}} e^{\pm \partial/\partial n}$  which alter pair number by  $\pm 1$ . When rewritten in terms of these exponential operators, the Josephson contribution reduces to its more familiar sinusoidal form

$$\mathbf{H}_{\text{junction}} = -\frac{E_J}{2} \left[ e^{-i\phi} + e^{i\phi} \right] = -E_J \cos \phi.$$

The sum of the inductance, capacitance and junction terms yields the SQUID Hamiltonian

$$\mathbf{H}_{\text{SQUID}} = E_c \mathbf{n}^2 + \frac{(\Phi_0/2\pi)^2}{2L} (\phi - \phi_0)^2 - E_J \cos \phi.$$

The equations of motion following from this Hamiltonian

$$\frac{d\mathbf{n}}{dt} = \frac{i}{\hbar} [\mathbf{H}_{\text{SQUID}}, \mathbf{n}] \quad (5.6a)$$

$$\frac{d\phi}{dt} = \frac{i}{\hbar} [\mathbf{H}_{\text{SQUID}}, \phi] \quad (5.6b)$$

are readily evaluated using the commutation relations listed in Appendix A. From (5.6a), we obtain a quantum version of Kirchoff's current conservation law

$$\mathbf{I}_{\text{capacitance}} + \mathbf{I}_{\text{inductance}} + \mathbf{I}_{\text{junction}} = 0 \quad (5.7)$$

with

$$\mathbf{I}_{\text{capacitance}} = \frac{d\mathbf{Q}}{dt} = 2e \frac{d\mathbf{n}}{dt} \quad (5.8a)$$

$$\mathbf{I}_{\text{inductance}} = \frac{\Phi_{\text{total}} - \Phi_{\text{ext}}}{L} = \frac{(\Phi_0/2\pi)}{L} \phi \quad (5.8b)$$

$$\mathbf{I}_{\text{junction}} = \left( \frac{2\pi}{\Phi_0} \right) E_J \sin \phi \equiv I_c \sin \phi. \quad (5.8c)$$

Conservation relation (5.7) indicates that a SQUID can be modeled by the equivalent circuit pictured in fig. 10. The cross appearing in the figure represents the Josephson junction and its supercurrent flow (5.8c) which depends upon the phase drop across the junction.

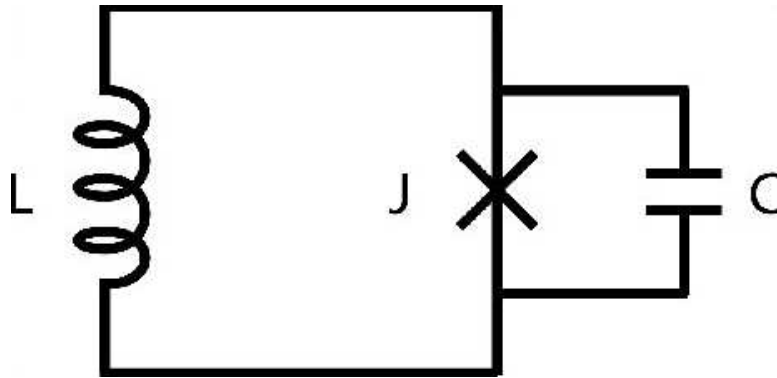


Fig. 10: Equivalent circuit for a SQUID containing an inductor  $L$  and Josephson junction  $J$ . The junction's capacitance is modeled by capacitor  $C$ .

So long as  $I_{\text{junction}}$  remains less than the critical value  $I_c \equiv (2\pi/\Phi_0)E_J$ , the supercurrent tunnels through the insulator without dissipation. The voltage counterpart to  $I_{\text{junction}}$  also depends upon the phase drop  $\phi$ , and it is obtained from the second equation of motion in (5.6b):

$$\mathbf{V}_{\text{junction}} = \left(\frac{\Phi_0}{2\pi}\right) \frac{d\phi}{dt}. \quad (5.9)$$

The Josephson junction's I-V characteristics are governed by eqns. (5.8c) and (5.9).

We make two final comments about  $\mathbf{H}_{\text{SQUID}}$ . Firstly, it is customary to introduce the dimensionless parameter

$$\beta_L \equiv \frac{LI_c}{(\Phi_0/2\pi)} = L \left(\frac{2\pi}{\Phi_0}\right)^2 E_J$$

which counts the number of “fluxons” that thread the SQUID ring when it carries critical current  $I_c$ . When parameter  $L$  is eliminated in favor of  $\beta_L$ , the Hamiltonian in the  $\phi$  representation reduces to

$$H_{\text{SQUID}} = -E_C \frac{\partial^2}{\partial \phi^2} + E_J \left[ \frac{(\phi - \phi_0)^2}{2\beta_L} - \cos \phi \right]. \quad (5.10)$$

Secondly, we scale out capacitance energy  $E_C$  from  $H_{\text{SQUID}}$  for simulation purposes. The dimensionless SQUID Hamiltonian then takes the same form as the template in (2.2)

$$\mathcal{H} = -\frac{\partial^2}{\partial \phi^2} + \alpha U(\phi) \quad (5.11)$$

with coupling constant  $\alpha = E_J/E_C$  and potential

$$U = \frac{(\phi - \phi_0)^2}{2\beta_L} - \cos \phi. \quad (5.12)$$

## 5.2. SQUID response to a time dependent background <sup>4</sup>

The SQUID Hamiltonian is a function of the two free parameters  $\beta_L$  and  $\phi_0$  in addition to the overall coupling  $\alpha = E_J/E_C$ . If naive dimensional analysis intuition is to hold,  $\beta_L$  and  $\phi_0$  must both be of order unity. Their precise values control the potential's shape and thereby strongly influence one's ability to extract useful information from low lying

---

<sup>4</sup> After work on this article was completed, we learned that a similar analysis of SQUID response to a time dependent pulse was recently reported in ref. [17]. Where overlap exists, there is generally good agreement between the findings of ref. [17] and the results independently derived in this subsection.



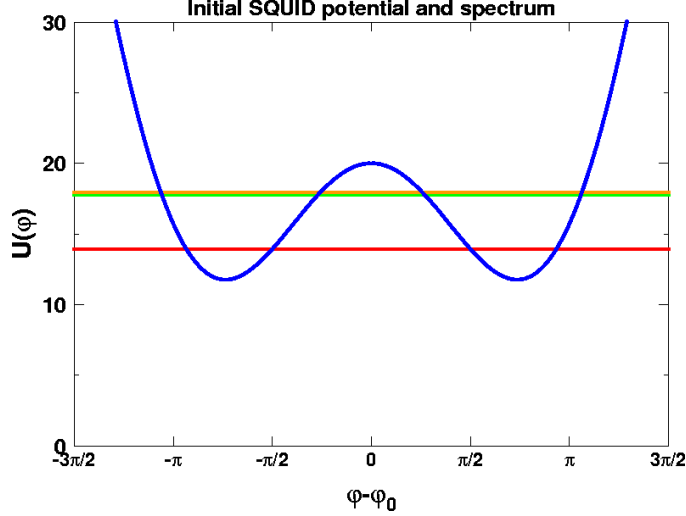


Fig. 11: Dimensionless SQUID potential corresponding to parameters  $\beta_L = \phi_0 = \pi$  and coupling  $\alpha = E_J/E_C = 10$ . The colored horizontal lines denote the system's lowest four energy eigenvalues. The splitting between the ground and first excited state energies is not resolvable on this plot's energy scale.

quantum states. We choose to fix  $\beta_L = \phi_0 = \pi$  so that the SQUID potential looks like a double-well centered about  $\phi = \phi_0$ . For simulation as well as visualization purposes, we also initially set  $\alpha = 10$ .  $U(\phi)$  is plotted for these parameter choices in fig. 11.

The Hamiltonian remains invariant under a discrete  $\phi - \pi \rightarrow -(\phi - \pi)$  symmetry, and the system's energy eigenstates are even and odd with respect to this parity operation. As the horizontal energy lines in fig. 11 demonstrate, the low lying parity partners are nearly degenerate:

$$\begin{aligned} E_0^{(+)} &= 13.8916 & E_0^{(-)} &= 13.8960 \\ E_1^{(+)} &= 17.7426 & E_1^{(-)} &= 17.9174. \end{aligned} \tag{5.13}$$

These energy eigenvalues establish relevant time scales for the design of a quantum NOT gate. For example, suppose the SQUID is initially prepared in the state  $\psi = (\psi_0^{(+)} + \psi_0^{(-)})/\sqrt{2}$  which is localized in the positive well and corresponds to a counterclockwise current. In half a beat period  $0.5 T_{\text{beat}} = \pi/(E_0^{(-)} - E_0^{(+)}) = 714$ , the system naturally tunnels into the negative well, and the current flows in a clockwise direction. Intentional switching of the SQUID's wavefunction must obviously be performed and measured on a much shorter time scale. <sup>5</sup>

---

<sup>5</sup> In this notional NOT gate example, we make no attempt to model decoherence effects which

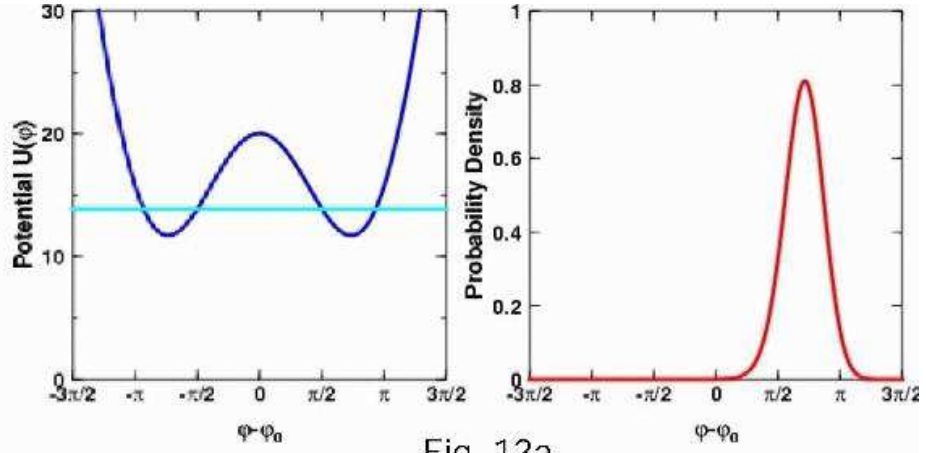
$\tau=0$ 

Fig. 12a

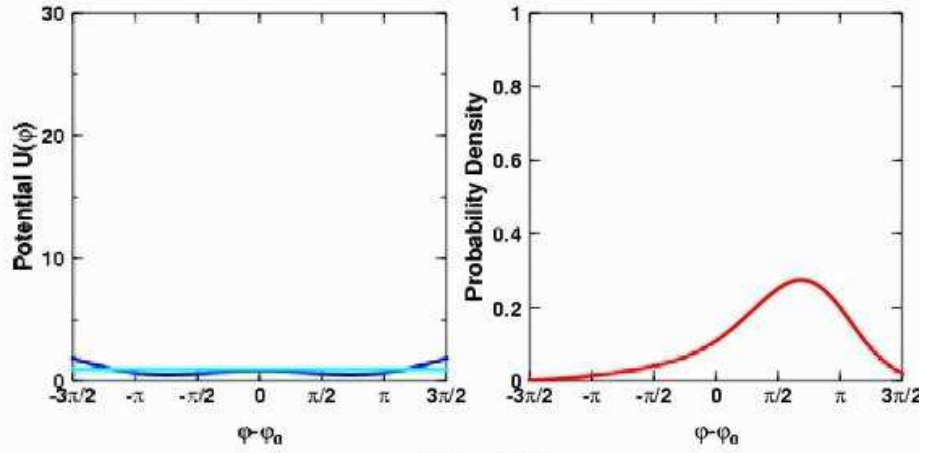
 $\tau=7.5$ 

Fig. 12b

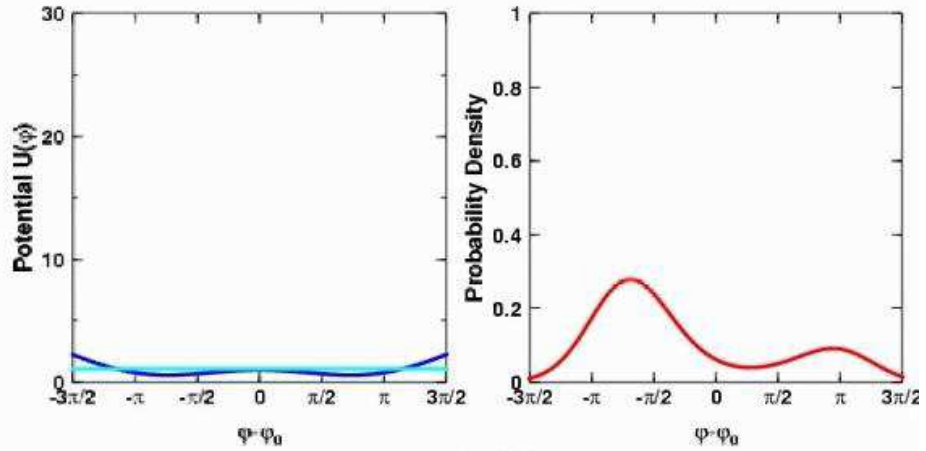
 $\tau=15$ 

Fig. 12c

are present in any real-world quantum experiment. But it is important to realize that the decoherence time could well set a much more stringent upper bound on when a measurement must be performed than does  $0.5 T_{\text{beat}}$ .

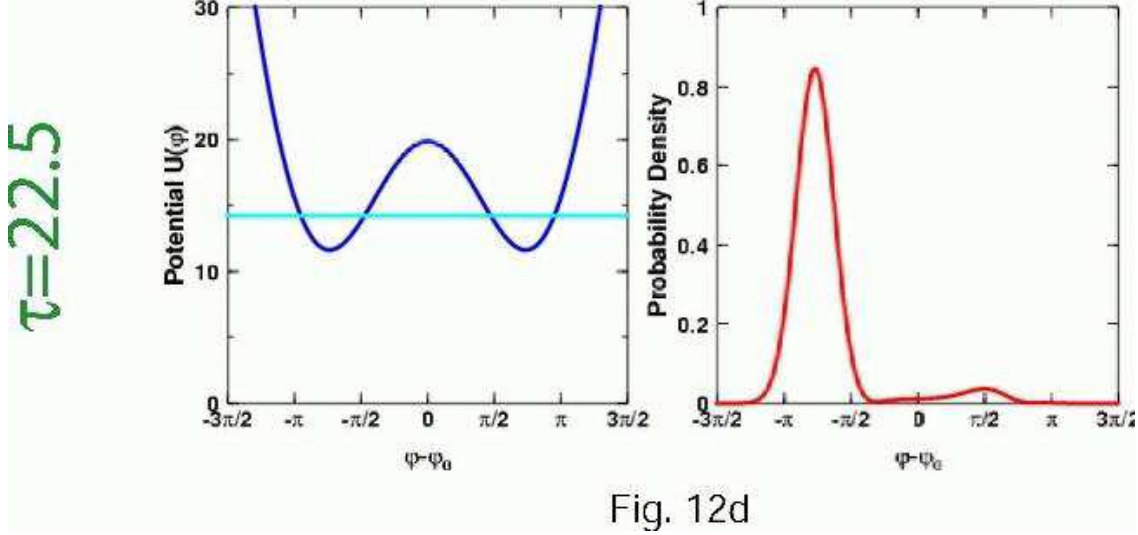


Fig. 12d

Fig. 12: Snapshots of the dimensionless potential for a SQUID with  $\beta_L = \phi_0 = \pi$  and variable  $\alpha$ . The light blue horizontal lines represent the system's time dependent energy. The evolution of the SQUID's probability density illustrates the system's response to the background.

The energy of the initial state as well as its probability density are graphed in fig. 12a. As can be seen in the figure, the horizontal light blue line representing the state's energy lies significantly below the local center maximum of the SQUID potential. Probability density oscillation between the wells is classically forbidden, and it only slowly proceeds quantum mechanically. In order to increase the frequency of wavefunction beating, we need to lower the potential barrier. This reduction may be implemented by diminishing the coupling constant.

Modulating a SQUID's  $\alpha = E_J/E_C$  value can be experimentally achieved by subjecting the Josephson junction to an external magnetic field. The rate at which  $\alpha$  is modified is constrained by the information theory requirement that high energy SQUID states not be unduly excited. In particular, we do not want the potential's time dependence to introduce excitations which are much more energetic than the separation

$$\Delta E_{10} \equiv \frac{E_1^{(+)} + E_1^{(-)}}{2} - \frac{E_0^{(+)} + E_0^{(-)}}{2}$$

between the zeroth and first pairs of SQUID eigenstates. This second relevant energy scale provides an order-of-magnitude estimate  $\tau_{\text{trans}} \approx 2\pi/\Delta E_{10} = 1.6$  for the time during which  $\alpha$  should transition from its large initial value to a smaller intermediate size.

We next use our simulator to determine an intermediate coupling for which well-hopping becomes classically allowed. We find that if  $\alpha$  is reduced from 10 to 0.4 according to the schedule shown in fig. 13, the resulting SQUID energy lies slightly above the modified potential's barrier. The dashed vertical red lines in the figure depict the transition time  $\tau_{\text{trans}}$ . The potential, system energy and system probability density after the transition is complete are illustrated in fig. 12b. As we see from the eigenenergies for the  $\alpha = 0.4$  potential

$$\begin{aligned}\varepsilon_0^{(+)} &= 0.7377 & \varepsilon_0^{(-)} &= 0.9834 \\ \varepsilon_1^{(+)} &= 1.5514 & \varepsilon_1^{(-)} &= 2.1090,\end{aligned}\tag{5.14}$$

the splitting between the ground and first excited state is two orders of magnitude larger than that for its  $\alpha = 10$  counterpart. So the SQUID's probability density migrates nearly 100 times faster from one well to the other following the transition.

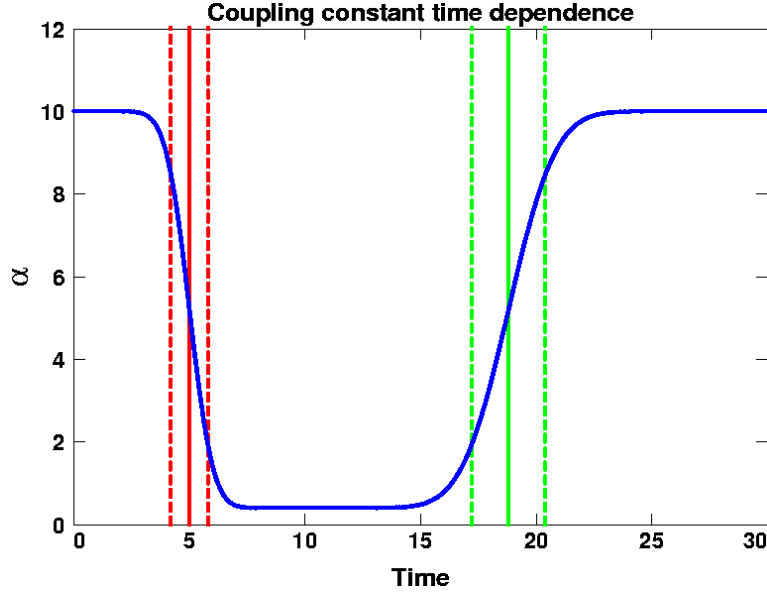


Fig. 13: SQUID coupling time dependence which induces NOT gate behavior:

$$\alpha(\tau) = 10 + \frac{10 - 0.4}{2} \left[ \text{erf} \left( \frac{\tau - 5}{0.8\sqrt{2}} \right) - \text{erf} \left( \frac{\tau - 13.8}{1.6\sqrt{2}} \right) \right].$$

After an interval approximately equal to one half of the new beat period  $0.5 T'_{\text{beat}} = \pi/(\varepsilon_0^{(-)} - \varepsilon_0^{(+)}) = 12.8$ , most of the SQUID's probability density resides within the negative

well (see fig. 12c). We then want to raise the barrier back to its original height in order to trap the bulk of the wavefunction in its new location. The separation

$$\Delta\varepsilon_{10} = \frac{\varepsilon_1^{(+)} + \varepsilon_1^{(-)}}{2} - \frac{\varepsilon_1^{(+)} + \varepsilon_1^{(-)}}{2}$$

between the zeroth and first pairs of  $\alpha = 0.4$  SQUID eigenstates again provides an order-of-magnitude upper bound for a reasonable second transition time  $\tau'_{\text{trans}} \approx 2\pi/\Delta\varepsilon_{10} = 6.5$ . After running several simulation tests, we find that taking  $\tau'_{\text{trans}} = 3.2$  leads to successful wavefunction capture with a final SQUID energy  $E_{\text{final}} = 14.3$  that is quite close to its original value  $E_{\text{init}} = 13.9$ . The timing and duration of the potential's return to its original form are depicted by the green lines in fig. 13. The system's probability density after the entire coherent operation is over is shown in fig. 12d.

A measurement made of the SQUID's final current sense is highly likely to be opposite to that of its initial direction. So driving the  $\alpha = E_J/E_C$  coupling according to a schedule like that in fig. 13 represents one possible way to implement a quantum NOT gate. It is interesting to note that all quantum computing logic can be built up from NOT gates as well as CNOT (controlled not) gates. SQUID implementations of CNOT have also been considered in the recent literature [18].

## 6. Conclusion

In this article, we have developed a new approach for numerically solving Schrödinger's equation, and we have used it to analyze the low energy behavior of several quantum systems. Our numerical algorithms are based upon a Baker-Campbell-Hausdorff expansion of the time evolution operator which manifestly preserves unitarity and works in any number of spatial dimensions. We have also identified a ratio of characteristic potential to kinetic energies as a key coupling constant  $\alpha$  that fixes the strength of the interaction between a quantum system and its classical background. For problems where  $\alpha$  represents the only dimensionless parameter whose value significantly exceeds unity, dimensional analysis establishes relevant length and time scales for low energy states. It is important to take the  $\alpha$  dependence of these physical scales into account when numerically integrating Schrödinger's equation.

We have applied our numerical techniques to compute energy eigenvalues and eigenstates for a number of examples. The methodology has been validated by reproducing

known answers for analytically soluble problems and computing consistent results for analytically intractable models. We have also simulated the evolution of bound states and propagating packets. Various quantum phenomena such as potential barrier tunneling, stationary state interference, and wavefunction diffusion have been graphically displayed. These illustrative examples help develop quantum intuition, especially when they clash with classical expectations.

Finally, we have demonstrated that our approach can be usefully applied to systems interacting with time dependent potentials. In particular, it provides a valuable tool for designing quantum information devices. Theoretical simulation of quantum circuits can help guide ongoing and future experiments which are important from both fundamental physics and technological standpoints. Indeed, this last point provided the impetus for this work.

In closing, we briefly mention a few applications of the methods and insights presented in this article which we believe will be interesting to pursue. One current outstanding challenge in quantum computing is to build a robust measuring apparatus that can read out a qubit's state without prematurely destroying its quantum information. SQUID technology is being pursued for not only qubit construction but also measurement operations. Preliminary simulations of such SQUID measuring circuits evince many of the same quantum issues as the more elementary examples discussed in this paper:  $\alpha = E_J/E_C$  values which are orders of magnitude larger than unity, initial wavefunctions which are concentrated in deep potential wells, temporal pulse shaping which is needed to avoid undue excitations, time scales for wavepacket mean motion which are longer than those for packet spreading, etc. Theoretical simulation and experimental implementation of SQUID measurement circuits will be reported elsewhere [19]. But clearly, many of the ideas discussed here can be usefully applied to exciting problems that lie at the quantum information processing frontier.

### Acknowledgments

We thank A. Bradley, T. Imbo, M. Misiak and W. Oliver for their helpful comments on the manuscript.

## Appendix A. Position and momentum space conventions

We collect together in this appendix various useful position and momentum eigenstate and operator identities in  $n$  spatial dimensions. We follow Feynman's approach to keeping track of where factors of  $2\pi$  appear in these relations. One factor of  $2\pi$  accompanies every momentum space delta function in each spatial dimension, while  $1/2\pi$  accompanies every momentum space measure factor. No other sources of  $2\pi$  enter into the identities below.

Eigenstate orthonormality relations:

$$\begin{aligned}\langle \vec{x} | \vec{x}' \rangle &= \delta^{(n)}(\vec{x} - \vec{x}') \\ \langle \vec{p} | \vec{p}' \rangle &= (2\pi)^n \delta^{(n)}(\vec{p} - \vec{p}')\end{aligned}$$

Eigenstate completeness relations:

$$\int d^n x |\vec{x}\rangle \langle \vec{x}| = \int \frac{d^n p}{(2\pi)^n} |\vec{p}\rangle \langle \vec{p}| = \mathbf{1}$$

Delta function identities:

$$\begin{aligned}\int d^n x e^{i\vec{x} \cdot (\vec{p} - \vec{p}')} &= (2\pi)^n \delta^{(n)}(\vec{p} - \vec{p}') \\ \int \frac{d^n p}{(2\pi)^n} e^{i\vec{p} \cdot (\vec{x} - \vec{x}')} &= \delta^{(n)}(\vec{x} - \vec{x}')\end{aligned}$$

Position and momentum eigenstate overlap:

$$\langle \vec{x} | \vec{p} \rangle = e^{i\vec{x} \cdot \vec{p}} \quad \langle \vec{p} | \vec{x} \rangle = e^{-i\vec{p} \cdot \vec{x}}$$

Fourier transform conventions:

$$\begin{aligned}\tilde{\psi}(\vec{p}) &= \int d^n x e^{-i\vec{p} \cdot \vec{x}} \psi(\vec{x}) \equiv \mathcal{F}(\psi(\vec{x})) \\ \psi(\vec{x}) &= \int \frac{d^n p}{(2\pi)^n} e^{i\vec{x} \cdot \vec{p}} \tilde{\psi}(\vec{p}) \equiv \mathcal{F}^{-1}(\tilde{\psi}(\vec{p})).\end{aligned}$$

Here  $\psi(\vec{x}) = \langle \vec{x} | \psi \rangle$  denotes a position space wavefunction, while  $\tilde{\psi}(\vec{p}) = \langle \vec{p} | \psi \rangle$  represents its momentum space counterpart.

Commutation relations:<sup>6</sup>

$$\begin{aligned}
[\vec{\mathbf{P}}, \vec{\mathbf{X}}] &= -i \\
[\vec{\mathbf{P}}, V(\vec{\mathbf{X}})] &= -i\nabla V(\vec{\mathbf{X}}) \\
[\vec{\mathbf{P}}^2, V(\vec{\mathbf{X}})] &= 2\{-i\nabla V(\vec{\mathbf{X}})\} \cdot \vec{\mathbf{P}} + (-i\nabla)^2 V(\vec{\mathbf{X}})
\end{aligned}$$

## Appendix B. Explicit but approximate $O(t^4)$ wavefunction evolution formula

After expanding all commutators in the time evolution operator  $\mathbf{U}(t)$  shown in (1.6), we let it act upon an initial state vector  $|\psi(0)\rangle$ :

$$\begin{aligned}
|\psi(t)\rangle &= e^{it^2\vec{\nabla}\cdot\vec{\mathbf{P}}} e^{\left[it^3\left(\frac{2}{3}\vec{\nabla}V\cdot\vec{\nabla}V+\frac{1}{6}\nabla^2\nabla^2V\right)+\frac{1}{2}t^2\nabla^2V-itV\right]} \\
&\times e^{\left[-\frac{2}{3}it^3\sum_j\mathbf{P}_j\nabla^2V\mathbf{P}_j-\frac{4}{3}it^3\sum_{j>k}(\partial_j\partial_jV)\mathbf{P}_j\mathbf{P}_k-it\vec{\mathbf{P}}^2\right]} |\psi(0)\rangle.
\end{aligned}$$

For computational speed purposes, we want to derive a wavefunction evolution formula that involves just one Fourier transform and one inverse transform. So we approximate  $\sum_j\mathbf{P}_j\nabla^2V\mathbf{P}_j \approx C\vec{\mathbf{P}}^2$  and  $\sum_{j>k}(\partial_k\partial_jV)\mathbf{P}_j\mathbf{P}_k \approx \sum_{j>k}C_{jk}\mathbf{P}_j\mathbf{P}_k$  for some potential-dependent constants  $C$  and  $C_{jk}$ . We then project the state vector onto the position basis to deduce

$$\begin{aligned}
\psi(\vec{x}, t) &\simeq e^{\left[it^3\left(\frac{2}{3}\vec{\nabla}V(\vec{x}')\cdot\vec{\nabla}V(\vec{x}')+\frac{1}{6}\nabla^2\nabla^2V(\vec{x}')\right)+\frac{1}{2}t^2\nabla^2V(\vec{x}')-itV(\vec{x}')\right]} \\
&\times \mathcal{F}^{-1}\left[e^{-\frac{4}{3}it^3\sum_{j>k}C_{jk}p_jp_k-\left(\frac{2}{3}Cit^3+it\right)\vec{p}^2}\mathcal{F}(\psi(\vec{x}, 0))\right] + O(t^4)
\end{aligned}$$

where  $\vec{x}' = \vec{x} + t^2\vec{\nabla}V(\vec{x})$ .

---

<sup>6</sup> Recall that the commutator of two hermitian operators always equals an anti-hermitian combination of operators.



## References

- [1] M.D. Feit, J.A. Fleck, Jr. and A. Steiger, J. Comput. Phys. **47** (1982) 412.
- [2] H. DeRaedt, Comput. Phys. Rev. **7** (1987) 1.
- [3] W.H. Press, S.A. Teukolsky, W.T. Vetterling and B.P. Flannery, *Numerical Recipes in C*, (Cambridge University Press, 1992) p. 851.
- [4] A.D. Bandrauk and H. Shen, J. Chem. Phys. **99** (1993) 1185.
- [5] A.D. Bandrauk and H. Shen, J. Phys. A **27** (1994) 7147.
- [6] C. Leforestier *et al.*, J. Comput. Phys. **94** (1991) 59.
- [7] G. Blanch, “Mathieu Functions”, in *Handbook of Mathematical Functions*, ed. M. Abramowitz and I.A. Stegun (Dover Publications, New York, 1970), p. 721.
- [8] A.J. Leggett, Prog. Theor. Phys. Supp. **69** (1980) 80
- [9] A.J. Leggett, Contemp. Phys. **25** (1984) 583.
- [10] J.R. Friedman, V. Patel, W. Chen, S.K. Tolpygo and J.E. Lukens, Nature **406** (2000) 43.
- [11] C.H. van der Wal, A.C.J. ter Haar, F.K. Wilhelm, R.N. Schouten, C.J.P.M. Harmans, T.P. Orlando, S. Lloyd and J.E. Mooij, Science **290** (2000) 773.
- [12] I. Chiorescu, Y. Nakamura, C.J.P.M. Harmons and J.E. Mooij, Science **299** (2003) 1869.
- [13] B.D. Josephson, Phys. Lett. **1** (1962) 251.
- [14] R.P. Feynman, R.B. Leighton and M. Sands, *The Feynman Lectures on Physics*, Vol III, Addison-Wesley (Reading) 1965, p. 21-8.
- [15] D.V. Averin, Fortschritte der Physik, **48** (2000) 1055
- [16] Y. Makhlin, G. Schön and A. Shnirman, Rev. Mod. Phys. **73** (2001) 357.
- [17] M. Crogan, S. Khlebnikov and G. Sadiek, Supercond. Sci. Technol, **15** (2002) 8.
- [18] V. Corato, P. Silvestrini, L. Stodolsky and J. Wosiek, Phys. Lett. A **309** (2003) 206.
- [19] K. Berggren, W. Oliver, J. Sage, P. Cho, in preparation.